Astronomy & Astrophysics

New *XMM-Newton* observation of the Phoenix cluster: properties of the cool core

P. Tozzi[1], F. Gastaldello[2], S. Molendi[2], S. Ettori[3,4], J. S. Santos[1], S. De Grandi[5], I. Balestra[6], P. Rosati[7,1], B. Altieri[8], G. Cresci[1], F. Menanteau[9,10], and I. Valtchanov[8]

[1] INAF, Osservatorio Astrofisico di Firenze, Largo Enrico Fermi 5, 50125 Firenze, Italy
e-mail: ptozzi@arcetri.astro.it
[2] INAF, IASF Milano, via E. Bassini 15, 20133 Milano, Italy
[3] INAF, Osservatorio Astronomico di Bologna, viale Berti Pichat 6/2, 40127 Bologna, Italy
[4] INFN, Sezione di Bologna, viale Berti Pichat 6/2, 40127 Bologna, Italy
[5] INAF, Osservatorio Astronomico di Brera, via E. Bianchi 46, 23807 Merate, Italy
[6] INAF, Osservatorio Astronomico di Trieste, via G.B. Tiepolo 11, 34131 Trieste, Italy
[7] Università degli Studi di Ferrara, via Savonarola, 9 – 44121 Ferrara , Italy
[8] European Space Astronomy Centre (ESAC), European Space Agency, Apartado de Correos 78, 28691 Villanueva de la Cañada, Madrid, Spain
[9] National Center for Supercomputing Applications, University of Illinois at Urbana-Champaign, 1205 W. Clark St., Urbana, IL 61801, USA
[10] Department of Astronomy, University of Illinois at Urbana-Champaign, W. Green Street, Urbana, IL 61801, USA

ABSTRACT

Aims. We present a spectral analysis of a deep (220 ks) *XMM-Newton* observation of the Phoenix cluster (SPT-CL J2344-4243). We also use *Chandra* archival ACIS-I data that are useful for modeling the properties of the central bright active galactic nucleus and global intracluster medium.

Methods. We extracted CCD and reflection grating spectrometer (RGS) X-ray spectra from the core region to search for the signature of cold gas and to finally constrain the mass deposition rate in the cooling flow that is thought to be responsible for the massive star formation episode observed in the brightest cluster galaxy (BCG).

Results. We find an average mass-deposition rate of $\dot{M} = 620\,(-190 + 200)_{\rm stat}\,(-50 + 150)_{\rm syst}\,M_\odot\,{\rm yr}^{-1}$ in the temperature range 0.3–3.0 keV from MOS data. A temperature-resolved analysis shows that a significant amount of gas is deposited at about 1.8 keV and above, while only upper limits on the order of hundreds of $M_\odot\,{\rm yr}^{-1}$ can be placed in the 0.3−1.8 keV temperature range. From pn data we obtain $\dot{M} = 210\,(-80 + 85)_{\rm stat}\,(-35 + 60)_{\rm syst}\,M_\odot\,{\rm yr}^{-1}$ in the 0.3−3.0 keV temperature range, while the upper limits from the temperature-resolved analysis are typically a factor of 3 lower than MOS data. No line emission from ionization states below Fe XXIII is seen above 12 Å in the RGS spectrum, and the amount of gas cooling below ∼3 keV has a formal best-fit value $\dot{M} = 122^{+343}_{-122}\,M_\odot\,{\rm yr}^{-1}$. In addition, our analysis of the far-infrared spectral energy distribution of the BCG based on *Herschel* data provides a star formation rate (SFR) equal to 530 $M_\odot\,{\rm yr}^{-1}$ with an uncertainty of 10%, which is lower than previous estimates by a factor 1.5. Overall, current limits on the mass deposition rate from MOS data are consistent with the SFR observed in the BCG, while pn data prefer a lower value of $\dot{M} \sim SFR/3$, which is inconsistent with the SFR at the 3σ confidence level.

Conclusions. Current data are able to firmly identify a substantial amount of cooling gas only above 1.8 keV in the core of the Phoenix cluster. At lower temperatures, the upper limits on $\dot{M}$ from MOS and pn data differ by a factor of 3. While the MOS data analysis is consistent with values as high as $\dot{M} \sim 1000$ within 1σ, pn data provide $\dot{M} < 500\,M_\odot\,{\rm yr}^{-1}$ at 3σ confidence level at a temperature below 1.8 keV. At present, this discrepancy cannot be explained on the basis of known calibration uncertainties or other sources of statistical noise.

Key words. galaxies: clusters: individual: SPT-CL J2344-4243 – galaxies: clusters: intracluster medium – X-rays: galaxies: clusters

1. Introduction

The majority of baryons in clusters of galaxies is constituted by virialized hot gas (Lin et al. 2003; Gonzalez et al. 2013) that emits X-ray via thermal bremsstrahlung. Temperature, density, and chemical composition of the so-called intracluster medium (ICM) can be directly measured thanks to X-ray imaging and spectroscopic observations. Spatially resolved spectroscopic studies showed a significant temperature decrease and strongly peaked surface brightness profiles in the center of a significant fraction of the cluster population. The short cooling times associated with these high-density gas regions led to the conclusion that a massive cooling flow was developing in the ICM in most of the clusters (Silk 1976; Cowie & Binney 1977; Fabian & Nulsen 1977; Mathews & Bregman 1978). The fate of this cooling gas would be to feed massive star formation episodes.

On the basis of the isobaric cooling-flow model (Fabian & Nulsen 1977; Fabian 1994), it was estimated that typical cooling flows may develop mass deposition rates in the range of a few $\times 100−1000\,M_\odot\,{\rm yr}^{-1}$. However, the lack of massive star formation events and of large reservoirs of cold gas at the

center of galaxy clusters casts some doubts on the hypothesis of a complete cooling of the ICM in cluster cores. The picture changed dramatically when X-ray observations, in particular of the RGS instrument onboard the *XMM-Newton* telescope, revealed a severe deficit of emission lines compared to the predictions of the isobaric cooling-flow model in all the groups and clusters of galaxies with putative cooling flows (Tamura et al. 2001; Peterson et al. 2001, 2003; Kaastra et al. 2001). Interestingly, this result has also been found in *XMM-Newton* and *Chandra* CCD spectra, despite the lower resolution, thanks to the prominent complex of iron L-shell lines (McNamara et al. 2000; Böhringer et al. 2001, 2002; Molendi & Pizzolato 2001). This directly implies that the cooling gas is present only in small amounts, typically ten times lower than expected for steady-state, isobaric radiative cooling (see Peterson & Fabian 2006). This determined a change from the cooling-flow paradigm, with typical deposition rates of about $100-1000\ M_\odot\ \mathrm{yr}^{-1}$, to the cool-core paradigm, where most of the gas is kept at temperatures higher than one-third of the ambient cluster temperature, and the mass deposition rate, if any, is due to a residual cooling flow of about few tens $M_\odot\ \mathrm{yr}^{-1}$.

Another direct implication of these observations is that there must be some process that heats the gas and prevents its cooling. Among the many mechanisms investigated in the past years, feedback from active galactic nuclei (AGN) is considered the most plausible heating source. Radio AGN are ubiquitous in cool cores (see Sun 2009), and interactions between the radio jets and the ICM have been observed unambiguously. AGN outbursts can in principle inject sufficient energy into the ICM (see McNamara et al. 2005). The relativistic electrons in jets associated with the central cluster galaxy are able to carve large cavities into the ICM. The free energy associated with these bubbles is plausibly transferred into the ICM and thermalized through turbulence (see McNamara & Nulsen 2012; Zhuravleva et al. 2014). In addition, there is increasing evidence of interactions of AGN outflows with metal-rich gas along the cavities and edges of radio jets of some individual clusters and groups (Kirkpatrick et al. 2011; Ettori et al. 2013b), consistent with numerical simulations showing that AGN outflows are able to advect ambient, iron-rich material from the core to a few hundred kpc away (e.g., Gaspari et al. 2011a,b). The feedback mechanism has been observed in its full complexity in nearby clusters such as Perseus (Fabian et al. 2003, 2006, 2011), Hydra A (McNamara et al. 2000), and a few other clusters (see Blanton et al. 2011).

In addition, the regular behavior of cool cores is not only observed in local clusters, but seems to hold up to high redshifts. High angular resolution observations of cool cores at $z \le 1$ performed by our group (Santos et al. 2010, 2012) showed that the radio feedback mechanism is already present at $z \sim 1$. Temperature and metallicity profiles in cool cores are broadly consistent with local ones, with a remarkable difference in the metal distribution that appears to be more concentrated in the core than in local clusters (De Grandi et al. 2014). This indicates that radio feedback also plays a role in the spatial distribution of metals. The regularity of the cool-core appearance over the entire cluster population and a wide range of epochs points toward a gentle heating mechanism, with the radio AGN acting with a short duty-cycle to counterbalance the onset of cooling flows since the very first stages of cluster formation. At the same time, outburst shocks may provide a more violent heating mechanism. It is poorly understood whether AGN heating of the ICM occurs violently through shocks or through bubbles in pressure equilibrium that cause turbulence. Outburst shock with jumps in temperature are very hard to detect, and shocks

have been unambiguously detected in only a few cases (see, e.g., A2052 and NGC 5813, Blanton et al. 2011; Randall et al. 2011). It is now widely accepted, however, that the mechanical energy provided by the AGN through jets is sufficient to overcome the cooling process in cluster cores. Therefore questions remain about the detailed physical mechanism that transfers energy to the ICM, and how this mechanism gives rise to the regular cool-core thermal structure, which requires a minimum temperature a factor ~ 3 lower than the ambient cluster temperature.

Surprisingly, a recent observation introduced further changes in the picture outlined here. The SZ-selected cluster SPT-CLJ2344-4243 (also known as the Phoenix cluster, McDonald et al. 2012) at $z \sim 0.596$ for the first time shows hints of a massive cooling-flow-induced starburst, suggesting that the feedback source responsible for preventing runaway cooling may not yet be fully established. SPT–CLJ2344-4243 shows a strong cool core with a potential mass deposition rate of $\sim 3000\ M_\odot\ \mathrm{yr}^{-1}$ derived from the X-ray luminosity. McDonald et al. (2012) argued that the Phoenix cluster might harbor an almost isobaric cooling flow with an unusually high mass deposition rate. The strongest hint comes from the very high star formation rate (SFR) observed in the brightest cluster galaxy (BCG), which has originally been estimated to be $\sim 700\ M_\odot\ \mathrm{yr}^{-1}$, with large 1σ errors ranging from 200 to 500 $M_\odot\ \mathrm{yr}^{-1}$ (McDonald et al. 2012). However, an accurate measurement of the SFR is made difficult by the presence of a strongly absorbed AGN, whose contribution to the BCG emission can be accounted for in different ways. Recently, the HST/WFC3 observation of the Phoenix (McDonald et al. 2013) showed filamentary blue emission out to 40 kpc and beyond, and the estimated, extinction-corrected SFR has been updated to a more accurate value of $798 \pm 42\ M_\odot\ \mathrm{yr}^{-1}$, consistent with optical and IR data at lower spatial resolution.

In this work we present the analysis of a 220 ks observation with *XMM-Newton* awarded in AO12 on the Phoenix cluster, with the main goal of investigating the thermal structure of the cool core and comparing the mass deposition rate in the core to the SFR in the BCG. We also use archival *Chandra* data (about 10 ks with ACIS-I) to model the emission of the AGN in the BCG and global ICM properties. Finally, we revise the SFR in the BCG on the basis of far-IR (FIR) data from the *Herschel* Observatory.

The paper is organized as follows. In Sect. 2 we describe the reduction of the *XMM-Newton* and *Chandra* data. In Sect. 3 we present the results from the *Chandra* data analysis on the central AGN spectrum and the global ICM properties. In Sect. 4 we describe our analysis strategy and present the results on the cool-core temperature structure from EPIC MOS and pn data, RGS data, and *Chandra* data. In Sect. 5 we revise the measurement of the SFR in the BCG from FIR data in view of a comparison with the mass deposition rate. Finally, our conclusions are summarized in Sect. 6. Throughout the paper, we adopt the seven-year WMAP cosmology with $\Omega_\Lambda = 0.73$, $\Omega_\mathrm{m} = 0.27$, and $H_0 = 70.4\ \mathrm{km\,s^{-1}\ Mpc^{-1}}$ (Komatsu et al. 2011). Quoted errors and upper limits always correspond to a 1σ confidence level, unless stated otherwise.

2. Data reduction

2.1. XMM-Newton: EPIC data

We obtained a total of 225 ks with *XMM-Newton* on the Phoenix cluster in AO12[1]. Data were acquired in November and

---

[1] Proposal ID 72270, *The thermal structure of the cool core in the Phoenix cluster*, P.I. P. Tozzi.

Table 1. *XMM-Newton* data: exposure times for each Obsid after data reduction.

Obsid	EPIC detector	Effective t_{exp} ks
0722700101	MOS1	128.0
0722700101	MOS2	128.0
0722700101	pn	103.0
0722700201	MOS1	92.0
0722700201	MOS2	92.0
0722700201	pn	81.5
0693661801	MOS1	16.0
0693661801	MOS2	16.5
0693661801	pn	8.6

December 2013 (Obsid 0722700101, 132 ks, and 0722700201, 93 ks). We added a shorter 20 ks archival observation taken in 2012 to our analysis[2].

The observation data files (ODF) were processed to produce calibrated event files using the most recent release of the *XMM-Newton* Science Analysis System (SAS v14.0.0), with the calibration release XMM-CCF-REL-323, and running the tasks EPPROC and EMPROC for the pn and MOS, respectively, to generate calibrated and concatenated EPIC event lists. Then, we filtered EPIC event lists for bad pixels, bad columns, cosmic-ray events outside the field of view (FOV), photons in the gaps (FLAG=0), and applied standard grade selection, corresponding to PATTERN <12 for MOS and PATTERN <=4 for pn. We removed soft proton flares by applying a threshold on the count rate in the $10-12$ keV energy band. To define low-background intervals, we used the condition $RATE \leq 0.35$ for MOS and $RATE \leq 0.4$ for pn. We found that for Obsid 0722700101, we have about 128 ks for MOS1 and MOS2 and 103 ks for pn after data reduction. For Obsid 0722700201 we have 92 ks for MOS1 and MOS2 and 81.5 ks for pn. This means that removing high-background intervals reduces the effective total time from 225 ks to 220 for MOS (a loss of 2% of the total time) and to 184.5 ks for pn (a loss of 18% of the total time). The archival data, Obsid 0693661801, were affected by flares by a larger amount. From 20 ks of exposure in Obsid 0693661801, we have 16 and 16.5 ks for MOS1 and MOS2, respectively (a loss of about $18-20\%$), and 8.6 ks for pn (a loss of about 60% of the total time).

For each Obsid we merged the event files MOS1 and MOS2 to create a single event file. This procedure has been adopted because the MOS cameras typically yield mutually consistent fluxes over their whole energy bandpass[3]. Finally, we also removed out-of-time events from the pn event file and spectra. In Table 1, we list the resulting clean exposure times for the pn and the MOS detectors for the three exposures used in this work.

Effective area and response matrix files were generated with the tasks `arfgen` and `rmfgen`, respectively, for each obsid. For MOS, effective area and response matrix files were computed for each detector and were eventually summed with a weight corresponding to the effective exposure time of MOS1 and MOS2.

2.2. XMM-Newton: RGS data

We reduced the RGS data set using the standard SAS v14.0.0 pipeline processing through the RGSPROC tool. We filtered soft proton flares by excluding time periods where the count rate

---

[2] Proposal ID 069366, P.I. M. Arnaud.
[3] See http://xmm2.esac.esa.int/docs/documents/CAL-TN-0018.pdf.

Table 2. Cleaned exposure times for RGS detectors.

Obsid	RGS detector	Effective t_{exp} ks
0722700101	RGS1	126.4
0722700101	RGS2	125.2
0722700201	RGS1	92.4
0722700201	RGS2	92.7

on CCD9[4] is lower than 0.1 cts/s in a region free of source emission. The resulting effective exposure times, after removing flares from the data, are listed in Table 2. As background we adopted the model background spectrum created by the SAS task RGSBKGMODEL, which can be applied to a given observation from a combination of observations of empty fields, based on the count rate of the off-axis source-free region of CCD9. We verified that the background spectrum obtained in this way is entirely consistent with a local background extracted from beyond 98% of the RGS point spread function (PSF). Finally, we focused on the first-order spectra and combined spectra, backgrounds, and responses from all observations and from both RGS instruments using the SAS task RGSCOMBINE.

2.3. Archival Chandra data

The Phoenix cluster has been observed with ACIS-I for 11.9 ks in the VFAINT mode (Obsid 13401)[5]. We performed a standard data reduction starting from the level = 1 event files, using the `CIAO 4.6` software package, with the most recent version of the *Chandra* Calibration Database (`CALDB 4.6.3`). We ran the task `acis_process_events` to flag background events that are most likely associated with cosmic rays and removed them. With this procedure, the ACIS particle background can be significantly reduced compared to the standard grade selection. The data were filtered to include only the standard event grades 0, 2, 3, 4, and 6. We visually checked for hot columns that were left after the standard reduction. As expected for exposures taken in VFAINT mode, we did not find hot columns or flickering pixels after filtering out bad events. Finally, we filtered time intervals with high background by performing a 3σ clipping of the background level using the script `analyze_ltcrv`. Only a negligible fraction of the exposure time was lost in this step, and the final effective exposure time is 11.7 ks. We remark that our spectral analysis will not be affected by possible undetected flares, since we are able to compute the background in the same observation from a large source-free region close to the cluster position, thus taking into account any possible spectral distortion of the background itself induced by the flares.

3. Spectral analysis of *Chandra* data: AGN spectrum and global ICM properties

We first performed the spectral analysis of the *Chandra* data. Despite the short exposure time[6], the high angular resolution of

---

[4] This is the CCD that generally records the fewest source events because of its location close to the optical axis and is the most susceptible to proton events.
[5] Proposal ID 13800933, *"Chandra Observation of the Most Massive Galaxy Clusters Detected in the South Pole Telescope Survey"*, PI. G. Garmire.
[6] A new 100 ks observation with *Chandra* has been taken in August 2014, P.I. M. McDonald.

Chandra can provide important parameters useful in the spectral analysis of the *XMM-Newton* data. In particular, it is immediately clear from the high-resolution hard-band image that the BCG of the Phoenix cluster hosts a powerful obscured AGN. In *XMM-Newton* data, the point spread function has an half-energy width (HEW) of about 15″ at the aimpoint, which causes the AGN emission to be spread over the entire starburst region. *Chandra* data allow us to accurately measure the spectrum of the central AGN and eventually model its emission in the analysis of the XMM data.

We extracted a circular region with a radius of 1.5 arcsec to analyze the position of the central source in the hard-band *Chandra* image (RA = 23:44:43.9, Dec = −42:43:12.64). At variance with most cool core clusters, the AGN in the center of the Phoenix is extremely X-ray luminous. We only considered the energy range 1.0−10 keV for fitting purposes to avoid residual contamination from the thermal emission of the ICM. We detected 575 net counts in the 1.0−7 keV band, most of them in the hard 2−7 keV band. In our fit we fixed the redshift to the optical value $z_{opt} = 0.596$ (see McDonald et al. 2012). We also fixed the Galactic absorption to the value $NH_{Gal} = 1.52 \times 10^{20}$ cm^{-2} obtained from the radio map of Kalberla et al. (2005) at the position of the cluster. The AGN was modeled as a power law with an intrinsic absorption (*XSPEC* model zwabs × pow) convolved by the Galactic absorption model (tbabs). The slope of the power law was frozen to the value $\Gamma = 1.8$.

We found and intrinsic absorption $NH = (46\pm7)\times10^{22}$ cm^{-2} and unabsorbed intrinsic luminosities of $(3.1 \pm 0.1) \times 10^{45}$ and $(4.8 \pm 0.2) \times 10^{45}$ erg s^{-1} in the 0.5−2 keV and 2−10 keV bands, respectively. The *Chandra* spectrum of the AGN and the best-fit model are shown in Fig. 2. According to this, the central AGN can be classified as a type II QSO. These results are consistent with the results of Ueda et al. (2013), who found $NH = (32 \pm 9) \times 10^{22}$ cm^{-2} and $\Gamma = 1.54 \pm 0.27$ from the combined analysis of *Suzaku* XIS and HXD and *Chandra* (with CALDB 4.5.3). We also note that if we left Γ free in our fit, we found a much flatter spectrum with an intrinsic absorption lower by a factor of two, in agreement with the findings of Ueda et al. (2013) for the *Chandra* data alone. This is due to the well-known degeneracy between spectral slope and intrinsic absorption. Given the very low value ∼0.6 for the intrinsic spectral slope obtained in this way, we prefer to rely on the results with $\Gamma = 1.8$ consistent with the *Suzaku+Chandra* analysis. Since the contribution of the AGN in the soft band is crucial in our spectral analysis of the core region, we will eventually allow NH to range from 23 to 53×10^{22} cm^{-2}, to span the upper and lower 1σ limits of the two measurements in the analysis of the XMM data. Finally, we note that we cannot clearly identify the neutral Fe line at 6.4 keV rest-frame when adding an unresolved line component. We also remark that our analysis of *Chandra* data was obtained by removing the surrounding ICM emission, and not by modeling the thermal and AGN components together as in Ueda et al. (2013).

The total ICM emission contributes about 6400 net counts in the 0.5−7 keV within a radius of about 650 kpc, beyond which the surface brightness reaches the background level. This enabled us to perform the spectral analysis in independent rings with slightly fewer than 1000 net counts each. The projected temperature and iron abundance profiles are shown in Fig. 1 in the left and right panels, respectively. The temperature profile clearly shows a prominent cool core with a decrease of at least a factor of 2 from 200 kpc to the inner 50 kpc. This is mirrored in the iron abundance profile as a clear peak toward the center, where the iron abundance reaches solar metallicity (with solar
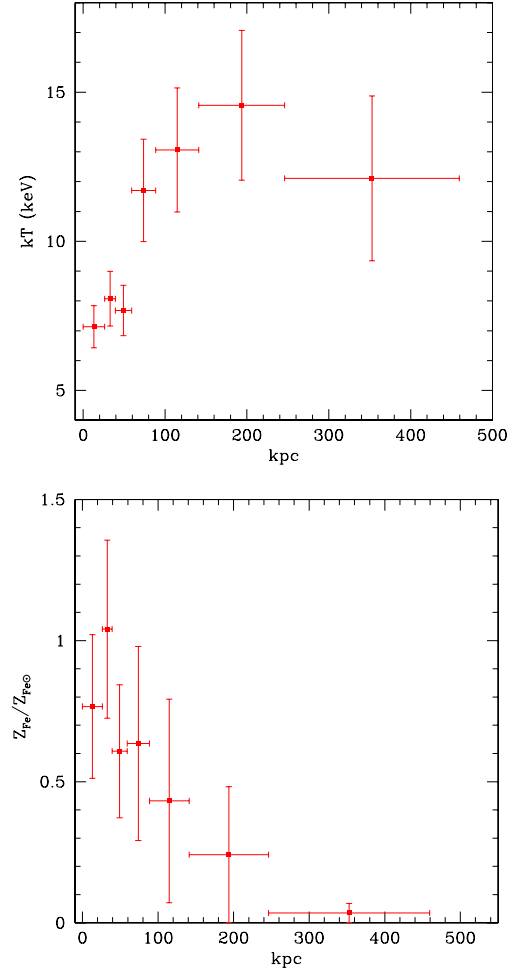

Fig. 1. *Top panel*: projected temperature profile of SPT-CLJ2344 obtained from the 11.7 ks *Chandra* ACIS-I observation, after removing the central AGN. Errorbars correspond to 1σ. *Bottom panel*: projected iron abundance profile of SPT-CLJ2344 from *Chandra* data.

metallicity values measured by Asplund et al. 2005) with an uncertainty of 30%. These results were used to complement the spectral analysis of *XMM-Newton* data.

We also computed the deprojected temperature and density profiles with a backward method (see Ettori et al. 2010, 2013a), which makes use of the geometrically deprojected X-ray surface brightness and temperature profiles to reconstruct the hydrostatic mass profile. This is assumed to be described by the NFW functional form (Navarro et al. 1996). The best-fit parameters of the mass profile were obtained through the minimization of the χ^2 statistics defined as the sum of the squared differences between the observed temperature and the temperature estimates obtained by inverting the equation of the hydrostatic equilibrium, weighted by the observational errors on the spectroscopic temperature. The gas density was derived from the deprojected surface brightness and the total mass model. With this method we measured a total mass, under the assumption of hydrostatic equilibrium, of $M_{500} = (2.34 \pm 0.71) \times 10^{15} M_\odot$ at $R_{500} = 1627 \pm 235$ kpc. The ICM mass within R_{500} is $M_{ICM} = (2.1 \pm 0.2) \times 10^{14} M_\odot$. From this, we obtained an ICM fraction of $f_{ICM} = 0.09 \pm 0.03$ at R_{500}. As a simple check, we estimated the parameter $Y_X = (27.3 \pm 4.1) \times 10^{14}$ keV $M_\odot$ assuming as representative of the entire cluster the temperature measured between 100 and 500 kpc, and computed the mass estimate from Y_X assuming the relation described in Arnaud et al. (2010) with
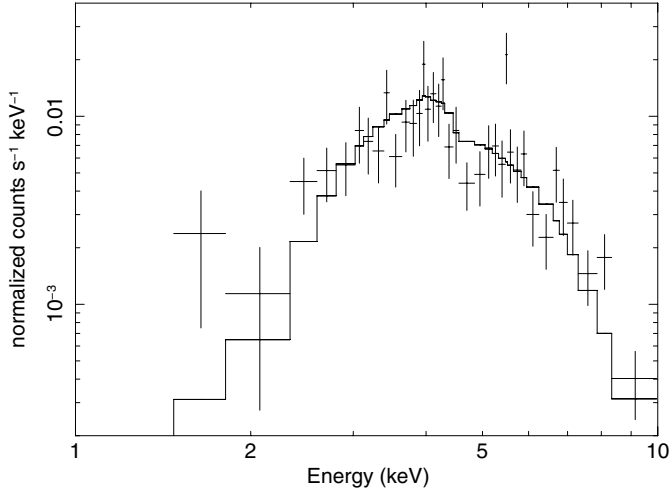
Fig. 2. Folded spectrum with best-fit model for the AGN in the center of the BCG of the Phoenix cluster. The spectrum is extracted from a radius of only 1.5 arcsec centered on the peak of the hard X-ray emission.

the slope fixed to the self-similar value. We found a mass of $(2.15 \pm 0.24) \times 10^{15} \, M_\odot$, consistent with the value previously computed from the hydrostatic equilibrium well within 1σ.

If we extrapolate the measured profile up to the virial radius adopting the best-fit NFW profile (Navarro et al. 1996), we find $M_{200} = 3.4 \pm 1.2 \times 10^{15} \, M_\odot$ at $R_{200} = 2500 \pm 400$ kpc. We note that this value is about a factor of 2 higher than the mass estimate $M_{200SZ} = (1.66 \pm 0.23_{\text{stat}} \pm 0.44_{\text{syst}}) \times 10^{15} \, M_\odot$ obtained from SZ-mass scaling relations in Williamson et al. (2011). However, considering that SZ-inferred masses are found to be statistically lower by a factor of 0.78 in their sample, the discrepancy between X-ray and SZ mass for the Phoenix is reduced to $\sim 1\sigma$, and therefore is not significant. Finally, by extrapolating the ICM density distribution, we find $M_{\text{ICM}} = (3.2 \pm 0.3) \times 10^{14} \, M_\odot$ for a virial ICM fraction of $f_{\text{ICM}} = 0.095 \pm 0.035$.

4. Spectral analysis of *XMM-Newton* data

4.1. Analysis strategy

We extracted the spectra from a circular region with a radius of 13.5 arcsec. This region was chosen to include the bulk of the emission from the core region, which is estimated to be confined within a radius of 40 kpc (about 6 arcsec at $z \sim 0.6$), plus 7.5 arcsec corresponding to the half-power diameter of the *XMM-Newton* PSF. Since the cold gas is expected to be concentrated toward the center of the cluster, we assumed that the signal from the cold gas emission outside this radius is negligible. This assumption is consistent with the results we obtained from the RGS spectra in two different extraction regions (see Sect. 4.3).

The background was sampled from a nearby region on the same CCD that was free from the cluster emission and was subtracted from the source spectrum. We note that the total background expected in the source region, computed by geometrically rescaling the sampled background to the source area, only amounts to 0.3% of the total observed emission. Before performing the final spectral analysis, we ran a few spectral fits artificially enhancing the background by factors of the order 1.2−1.5, which range encompasses any possible uncertainty in the background level. We found no relevant differences in the best-fit values as a function of the background rescaling factor. We conclude that the background only weakly affects the spectral analysis. We therefore only consider the results obtained

with the background sampled from the data and geometrically rescaled to the source region.

In *XMM-Newton* spectra the emission from the central AGN is mixed with the ICM emission, therefore we modeled its contribution with a power-law spectrum with a fixed slope of $\Gamma = 1.8$ and an intrinsic absorption ranging from 23 to 53 $\times$ 10^{22} cm^{-2} at the redshift of the cluster, as found in Sect. 3. We also left the normalization free for each separate spectrum to account for possible differences in the calibration of *Chandra* and *XMM-Newton*. We consistently found values in the range $(1.0−1.4) \times 10^{-3}$ for the normalization of the power-law component. The Galactic absorption, instead, was frozen to the value $NH_{\text{Gal}} = 1.52 \times 10^{20}$ cm^{-2} obtained from the radio map of Kalberla et al. (2005) at the position of the cluster, and it is described by the `tbabs` model. The effects of possible uncertainties on the Galactic absorption are discussed together with other systematic effects in Sect. 4.4.

We assumed that the gas in the residual cooling flow can be described by an isobaric cooling model, therefore we used the `mkcflow` spectral model (Mushotzky & Szymkowiak 1988). This model assumes a unique mass-deposition rate throughout the entire temperature range $T_{\min}−T_{\max}$. Since we are interested in the gas that is completely cooling and is continuously distributed across the entire temperature range, we set $T_{\min} = 0.3$ keV and $T_{\max} = 3.0$ keV. We set the lowest temperature to 0.3 keV because this is the lowest value that can possibly contribute to the emission in the *Chandra* and *XMM-Newton* energy range, given the relatively high redshift of the Phoenix cluster. However, a single `mkcflow` model may not be sufficient to investigate the structure of the cool core. The actual situation may be more complex, with some of the gas, above a given temperature threshold, cooling at a relatively high rate consistently with the isobaric cooling-flow model, while colder gas may have a much lower mass-deposition rate. Grating spectra of cool cores are traditionally fitted with an isobaric cooling-flow model with a cutoff temperature below which no gas is detected (Peterson & Fabian 2006). To explore a more complex scenario, we aimed at separately measuring the cooling rate (i.e., the mass deposition rate) in several temperature bins. In this case, the temperature intervals were fixed to 0.3−0.45, 0.45−0.9, 0.9−1.8, and 1.8−3.0 keV. This choice is similar to using the single-temperature `mekal` model for a discrete set of temperatures, but with the advantage of a continuous description of the gas instead of a set of discrete temperature values.

The contribution of the much hotter ICM component along the line of sight was modeled with a `mekal` model with a free temperature. Above 3 keV, a single-temperature `mekal` model can account for several hot components because it is not possible to resolve the temperature structure above 3 keV with the spectral analysis (see Mazzotta et al. 2004). This means that the possible contributions to the emission from temperatures between 3.0 keV (the highest temperature of the `mkcflow`) and the best-fit temperature of the `mekal` model are already described by a single-temperature `mekal` component. Therefore, despite the strong temperature gradient toward the center, the relevant part of the thermal structure of the ICM is properly treated by assuming a single temperature for the hot component and exploring the low-temperature regime with a multi-temperature `mkcflow` model.

In practice, our fitting method consists of two measurements of the mass deposition rates, using the following models:

– A single cooling-flow model `mkcflow` plus one single-temperature `mekal` component. The lowest temperature of
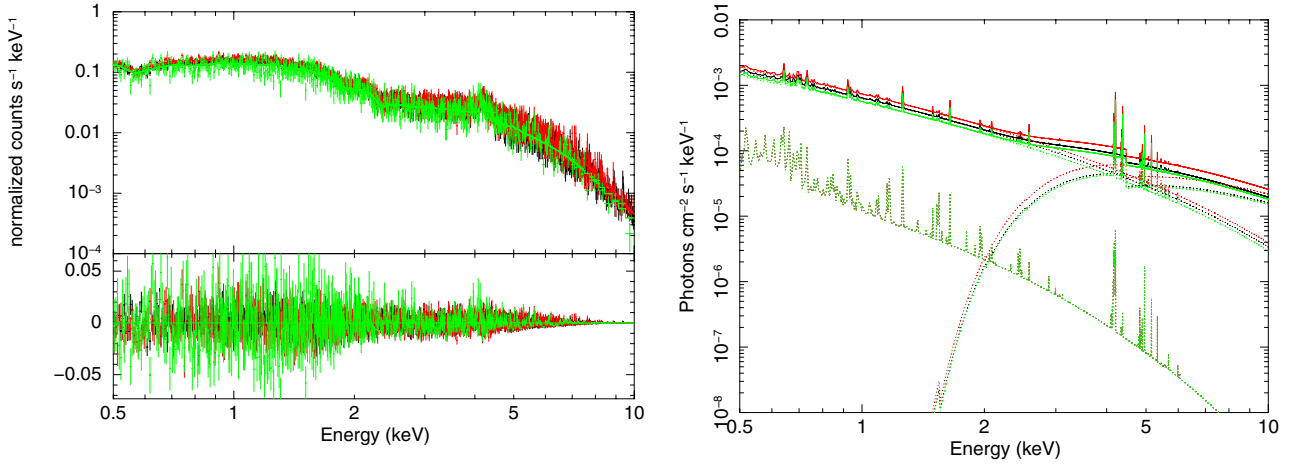
Fig. 3. *Left panel*: MOS spectra from the three Obsids with best-fit model obtained for a single `mkcflow` in the 0.3−3.0 keV temperature range. The *lower panel* shows the residual with respect to the best-fit model. *Right panel:* components of the best-fit model of the MOS spectra (three for each component, shown with dotted lines) obtained for a single `mkcflow` in the 0.3−3.0 keV temperature range. The `mkcflow` component is the lower thermal component, while the AGN contribution is virtually negligible below 2 keV.

the `mkcflow` component is frozen to 0.3 keV, and the largest to 3.0 keV. By setting the lowest temperature to 0.3 keV, we can interpret the normalization of the `mkcflow` model as the global deposition rate allowed for an isobaric cooling flow across the entire 0.3-3.0 keV temperature range. The redshift is tied to the best-fit value found in the hottest component. This choice does not introduce any uncertainty given the strong K_α line complex of the H-like and He-like iron.

- A set of `mkcflow` models whose lowest and highest temperatures are fixed to cover the 0.3−3.0 keV range with contiguous and not overlapping intervals. Here the normalization of each `mkcflow` component refers to the mass deposition rate in the corresponding temperature interval. The upper and lower temperatures are frozen to the following values: 0.3−0.45, 0.45−0.9, 0.9−1.8, and 1.8−3.0 keV. As in the previous case, a single-temperature `mekal` model accounts for any gas component hotter than 3 keV. The redshift is tied to the best-fit found in the hottest component here as well.

As a fitting method, we used the C-statistics, although we also ran our fits with the χ^2-statistics. In the latter case, spectra were grouped with at least a signal-to-noise ratio (S/N) of 4 in each bin. When running C-statistics, we used unbinned spectra (at least one photon per bin). As a default, we considered the energy range 0.5−10 keV both for the MOS and the pn data. We quote the best-fit values with 1σ error bars on the measured value of $\dot{M}$, or the 1σ upper limit. The same analysis was also applied to the *Chandra* data for a direct comparison.

4.2. Spectral results on the core region from EPIC MOS and pn data

Before fitting the XMM data, we performed a series of basic tests on our spectra. First, we separately fit pn and MOS spectra from each exposure using a single `mekal` model plus the fixed AGN component and Galactic absorption. The best-fit temperature values were all consistent within 1σ, showing that all the spectra are broadly consistent with each other. When we added a `mkcflow` component, we noted that the best-fit values of the mass deposition rates from pn data were lower than those from MOS data in all the different exposures. This shows that there may be significant differences between pn and MOS calibration that affect the measurements of cold gas components. Therefore, we proceeded with our standard analysis strategy,

which combines different exposures of the same detector, but fitted pn and MOS spectra separately.

Following our analysis strategy, first we separately fitted the MOS and pn data with a single `mkcflow` model, coupled with a `mekal` model to account for the hot ICM along the line of sight. We used both our new *XMM-Newton* data and the archival data. We considered the energy range 0.5−10 keV both for MOS and pn data. The *XSPEC* version used in this work is v12.8.1.

First we used a single `mkcflow` model with $T_{min} = 0.3$ keV and $T_{max} = 3.0$ keV to fit the combined MOS data with Cash statistics. The redshift of the cold gas component is linked to the best-fit redshift found for the hot component (described by a `mekal` model) $z_X = 0.593 \pm 0.002$, consistent with the optical value (McDonald et al. 2012). We found that the metal abundance of the `mkcflow` component is not constrained by the present data. Therefore we chose to explore the best-fit mass deposition rate by varying the cold gas metallicity Z_{cold} in a wide range of values. We set the lowest value for Z_{cold} equal to the metallicity measured for the hotter `mekal` component $Z_{hot} = 0.47^{+0.04}_{-0.03} Z_\odot$ (with solar metallicity values measured by Asplund et al. 2005), and we set the upper limit to the 2σ upper value ∼ 1.4 $Z_\odot$ found in the inner 80 kpc in the *Chandra* analysis. We quote the best-fit values obtained for $Z_{cold} = 1.0 Z_\odot$, and add the uncertainty associated to the range of Z_{cold} as a systematic error. We found a global mass deposition rate $\dot{M} = 620 (-190 + 200)_{stat} (-50 + 150)_{syst} M_\odot$ yr^{-1}. The intrinsic absorption of the AGN is found to be $NH = (42.0 \pm 1.5) \times 10^{22}$ cm^{-2}, in excellent agreement with the value found with the *Chandra* analysis. The best-fit temperature of the hot component is $kT_{hot} = (6.5 \pm 0.3)$ keV, which also agrees well with the emission-weighted temperature in the inner 80 kpc obtained from the analysis of the *Chandra* data. We repeated the fit with χ^2-statistics with spectra binned to at least an $S/N = 4$ per bin, and we found almost identical results, with a reduced $\chi^2 = 1.04$ for 663 d.o.f. The binned spectra of the three Obsids with the best-fit models are shown in Fig. 3, left panel. We show the different components of the best-fit model in the right panel of this figure. We note that the contribution of the cold gas in the temperature range 0.3−3 keV is about 5% in the 0.5−1 keV energy band, while the strongly absorbed AGN has virtually no emission below 2 keV, also when assuming the maximum uncertainty in the intrinsic absorption value. We conclude that the MOS data provide a positive detection of an average
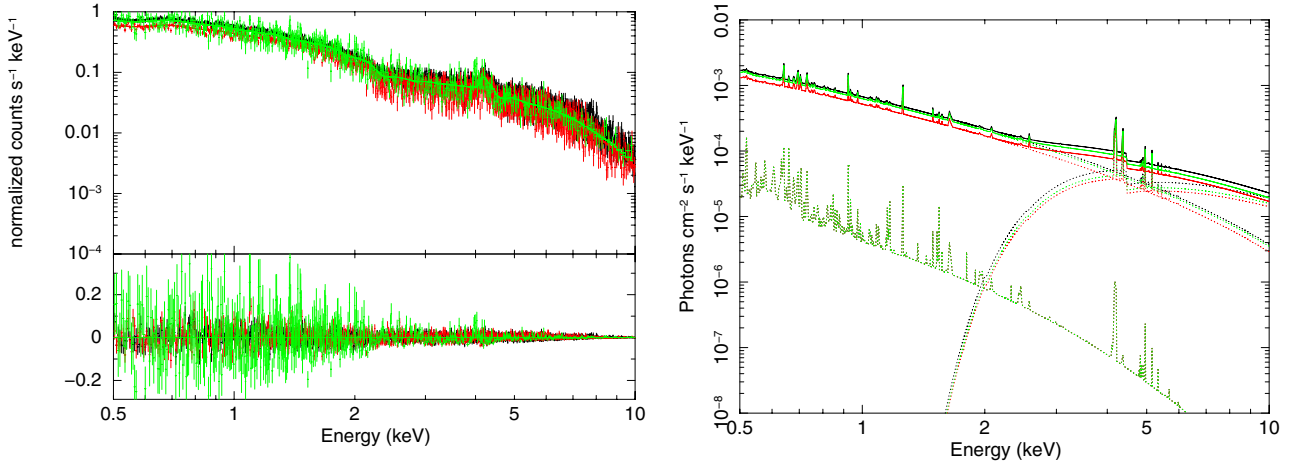
Fig. 4. *Left panel*: pn spectra from the three Obsids with best-fit model obtained for a single `mkcflow` in the 0.3−3.0 keV temperature range. The *lower panel* shows the residual with respect to the best-fit model. *Right panel:* components of the best-fit model of the pn spectra (three for each component, shown with dotted lines) obtained for a single `mkcflow` in the 0.3−3.0 keV temperature range. The `mkcflow` component is the lower thermal component, while the AGN contribution is virtually negligible below 2 keV.

mass-deposition rate in the temperature range 0.3−3.0 keV at the 3σ confidence level (c.l.), with $\dot{M} > 190\ M_\odot\ \text{yr}^{-1}$ at the 2σ c.l. after considering the systematic effect associated with the unknown metallicity of the cold gas. For completeness, we repeated our analysis without merging MOS1 and MOS2 spectra, which implies a combined fit of six independent spectra. We found similar results and error bars for all the parameters, with the best-fit values for the mass deposition rate lower by 6.5%.

Then we ran the multiple `mkcflow` model on the combined MOS spectra. The constraints on the amount of cold gas vary significantly as a function of the temperature range. In this case, the metal abundance of the cold gas is linked to the value found in the temperature range 1.8−3.0 keV, which is $Z_{1.8-3\ \text{keV}} = 0.36^{+0.19}_{-0.15}\ Z_\odot$. The best-fit temperature of the `mekal` component is now $kT_{\text{hot}} = 7.4^{+0.5}_{-0.4}$ keV with a metal abundance of $Z_{\text{hot}} = 0.54^{+0.05}_{-0.04}\ Z_\odot$. The results for $\dot{M}$ are shown in Fig. 5, top panel. We note that the lowest upper limits (at 1σ) are measured in the temperature bins 0.45−0.9 and 0.9−1.8 keV. These upper limits provide the strongest constraint for the fit with the single `mkcflow` model (see shaded area in Fig. 5). We also note that a clear detection of a mass deposition rate is obtained for the 1.8−3.0 keV temperature range. This means that our analysis of the MOS data with a temperature-dependent `mkcflow` model suggests that the cold gas around and below 1 keV does not cool as rapidly as the gas between 2 and 3 keV. This is consistent with the physical conditions often encountered in cool cores, where the gas cools down to a temperature floor below which it is hard to probe the presence of cooling gas. However, in the case of the Phoenix, the gas is observed to cool down to a temperature much lower than the ambient temperature T_{vir}, as opposed to the classic cool cores where the lowest temperature is $\sim 1/3 T_{\text{vir}}$. We only obtained upper limits on $\dot{M}$ for gas with temperatures below 2 keV. From comparing the results from the multi-temperature `mkcflow` model with that from the single-temperature `mkcflow`, we conclude that the mass deposition rate found in the analysis with a single `mkcflow` model should not be taken as representative of the entire cooling flow, since it is an emission-weighted value averaged over a temperature range that is too wide. Therefore, a temperature-resolved analysis of the cool core structure is mandatory to constrain the presence of a cooling flow. Nevertheless, the constraints on the

mass deposition rate from MOS data still allow values of several hundreds of $M_\odot\ \text{yr}^{-1}$, which might agree with the SFR observed in the BCG. Finally, the same fit on the separate MOS1 and MOS2 spectra provides very similar upper limits. In particular, the most constraining bin at $0.45 < kT < 0.90$ keV is left unchanged.

The fit of the pn data with the single `mkcflow` model encountered some difficulties. The best fit was obtained when the temperature of the hot component was $kT_{\text{hot}} = 5.9 \pm 0.1$ keV, which disagrees with the MOS data and with the *Chandra* results. In addition, the reduced $\chi^2 = 1.38$ for 637 degrees of freedom, is significantly larger than the value obtained for the MOS data. The lower temperature of the hot component is enough to account for most of the soft emission, which in the MOS fit was associated with the cold gas. As a result, the soft emission that can be associated with the cold gas is significantly lower, and the 3σ upper limit to the mass deposition rate is as low as $\sim 240\ M_\odot\ \text{yr}^{-1}$.

The significant difference between pn and MOS results clearly requires a detailed treatment of any cross-calibration uncertainty, which is beyond the goal of this paper. A first attempt to estimate the systematic uncertainty due to cross-calibration problems is discussed in Sect. 4.4. Nevertheless, a reliable assumption which may bring the two analyses into better agreement is to set the temperature of the hot gas to the value found with *Chandra* and *XMM-Newton* MOS, $kT_{\text{hot}} \sim 6.8$ keV. With this assumption, we find $\dot{M} = 210\ (-80\ + 85)_{\text{stat}}\ (-35\ + 60)_{\text{syst}}\ M_\odot\ \text{yr}^{-1}$. Here, the best-fit value was also obtained after freezing the abundance of the cold gas to $Z_{\text{cold}} = 1.0\ Z_\odot$, and the systematic error was obtained by varying the abundance of the cold gas in the range 0.45−1.4 $Z_\odot$. The abundance of the hot `mekal` component is $Z_{\text{hot}} = 0.48 \pm 0.04\ Z_\odot$, which agrees very well with the MOS data. Finally, the intrinsic absorption of the AGN is also well constrained to be $NH = (43.6 \pm 1.2) \times 10^{22}\ \text{cm}^{-2}$. The binned spectra of the three Obsids with the best-fit models are shown in Fig. 4, left panel. In Fig. 4, right panel, we show the different components of the best-fit model. It is possible to appreciate the lower `mkcflow` component with respect to the right panel of Fig. 3. This means that the analysis of the pn data plus the condition $kT_{\text{hot}} = 6.8$ keV provides a positive detection of a significant mass-deposition rate,
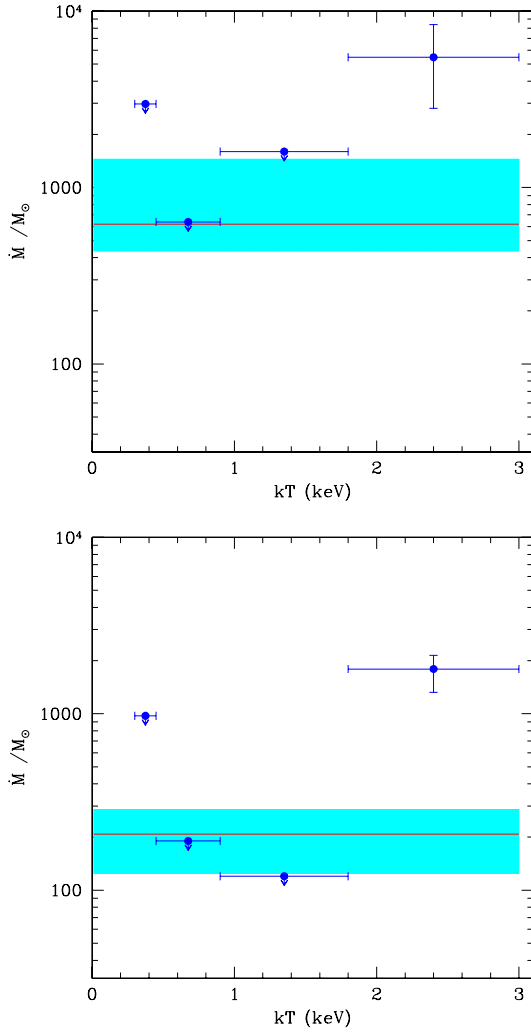
Fig. 5. *Top panel*: mass deposition rate $\dot{M}$ as a function of the temperature from the analysis of the MOS data of the Phoenix with a multi-component `mkcflow` model. Error bars are at 1σ confidence level and arrows represent upper limits at 1σ (the systematic uncertainty is not included here). The red horizontal line shows the best-fit value from the single `mkcflow` model in the 0.3–3.0 keV temperature range, while the shaded area shows the 1σ uncertainty. *Bottom panel*: same as in the top panel, but for the pn data.

although about a factor of 3 lower than those found in the MOS analysis.

We briefly comment on the dependence of $\dot{M}$ on the temperature of the surrounding hot gas. Clearly, the value of $\dot{M}$ critically depends on the amplitude of the continuum and therefore on the hot gas temperature. As already mentioned, our strategy consisted of anchoring the hot gas temperature to the best-fit value driven by the continuum in the high-energy range, while the colder gas below 3 keV was properly treated by the multi-temperature `mkcflow` model. With current data, any other treatment of the hot gas component would be highly speculative, therefore we did not explore the possible effect of the temperature distribution above 3 keV in the cluster core in more detail. We argue that the best way to deal with this aspect is to use highly spatially resolved data that allow avoiding the surrounding hot gas component as best possible and to focus on the innermost core region.

The analysis with a multi-temperature `mkcflow` model, shown in the bottom panel of Fig. 5, confirms this inconsistency.

The behavior of $\dot{M}$ as a function of the temperature is similar, with the most constraining upper limits coming from the temperature bins 0.45–0.9 and 0.9–1.8 keV and a clear detection of a high mass-deposition rate in the 1.8–3.0 keV temperature bin. The ratio between $\dot{M}$ in the bin 1.8–3.0 keV and the upper limits below 1.8 keV also has the same value as in the MOS analysis. We therefore qualitatively reach the same conclusion as was obtained from the MOS data analysis with the multi-temperature `mekal` model, but the values $\dot{M}$ are scaled down by a factor ~3. Incidentally, if the energy range used for spectral fitting is reduced to the 0.7–10.0 keV range, best-fit values and upper limits from the pn spectra are found to agree with MOS results. Clearly, this simply depends on the fact that the sensitivity to the cold gas is significantly reduced by excluding the energy bins below 0.7 keV, allowing much higher upper limits to the contribution from the cold gas.

To summarize, the analysis of *XMM-Newton* CCD spectra confirms the detection of gas cooling at a rate $>1000\ M_\odot\ yr^{-1}$ in the temperature range 1.8–3.0 keV, while it only provides upper limits for gas at temperatures $kT < 1.8$ keV. The upper limits to the global mass deposition rate below 1.8 keV appear to be consistent with an SFR of ~800 $M_\odot\ yr^{-1}$ within 1σ, as measured by McDonald et al. (2013) in the BCG, from the MOS data analysis. On the other hand, the upper limits on $\dot{M}$ measured from pn data at temperatures below 1.8 keV are significantly lower (more than 3σ) than the SFR. Therefore, no final conclusion can be drawn on the correspondence between the cooling flow and the observed SFR in the core of the Phoenix cluster.

4.3. Spectral results from RGS data

The RGS spectrum was extracted from a strip of roughly 50 arcsec long across the center of the object, a width corresponding to 90% PSF. Because the RGS is a slitless instrument and the zero-point of the wavelength calibration is dependent on the position of the detector in the field of view, we used as the source center the coordinates RA = 23:44:43.9, Dec = −42:43:12.64, which correspond to the position of the central AGN (see Sect. 3). In practice, with our choice for the extraction region, we collect photons from a box region with dimensions $50'' \times 12'$ centered on the source (see, e.g., Figs. 2 and 3 in Werner et al. 2009). This is the standard choice to maximize the signal from the cluster. This choice is motivated also by the fact that the Phoenix cluster has a brightness distribution that is similar to a point source from the XMM point of view, so that the line widening that is due to the spatial extension of the source does not severely affect the data. This means that the effective area that is sampled by our RGS spectrum is a circle with a radius of 25'', to be compared with the circle of 13'' used to extract the EPIC spectra. We also extracted an RGS spectrum from a narrower region with dimensions $15'' \times 12'$, corresponding to 70% of the PSF as opposed to the 98% of the PSF achieved with a width of 50''.

We fitted the first-order spectra between 7 and 27 Å, since this is the range where the source is higher than the background. We used *XSPEC* version 12.8.1 and C-statistic on the unbinned spectrum. We first applied a single-temperature `mekal` model modified by the Galactic absorption, while the redshift was fixed at the optical value. The AGN was modeled as in the fits of the EPIC data, but because of the strongly absorbed spectrum, the effect of the AGN emission is completely negligible in the RGS spectra given the limited wavelength range. From the RGS spectrum extracted from the larger regions (with a width of 50''), we found that a single-temperature model provides a reasonable fit to the data, with a $C_{stat}/d.o.f. = 1978/1952$ with a best-fit

Fig. 6. *Top panel*: combined RGS 1 and 2 spectrum for the Phoenix cluster and best-fit single-temperature model. The data have been rebinned to have a signal-to-noise ratio of 10 and divided by the effective area of the instrument only for displaying purpose. Relevant lines are also labeled. *Bottom panel*: The Phoenix spectrum (in red) is compared with the RGS spectrum of Abell 1835 (in black). We plot the fluxed spectra obtained with RGSFLUXER. Similar results are obtained by plotting the unfolded spectrum in *XSPEC* (the green line in the Phoenix spectrum) wit the only difference set by the binning condition $S/N = 10$. The best-fit thermal model of the Phoenix is also plotted as a blue line. We also plot relevant lines clearly seen in the spectra: the same sets of lines are present in both spectra in the overlapping wavelength range.

temperature of $kT = 6.2 \pm 0.4$ keV with a metal abundance of $Z = 0.55 \pm 0.09\ Z_\odot$. We show in the top panel of Fig. 6 the first-order combined spectrum with the best-fitting thermal model. In the same figure we show the positions of relevant emission lines that are clearly identifiable in the spectrum. The set of lines is the same seen in the RGS spectrum of the cluster Abell 1835, as shown in the comparison plot in the bottom panel of Fig. 6. For Abell 1835 we used the same data reduction as performed on the Phoenix data on the three observations not affected by flares (Obsid 0098010101, 0551830101, and 0551830201). The spectrum obtained with our reduction agrees very well with the spectrum shown by Sanders et al. (2010). Based on the RGS spectrum of the Phoenix cluster we therefore reach the same conclusions as were obtained for A1835: no line emission from

ionization states below Fe XXIII is seen above 12 Å, and no evidence for gas cooling below ~3 keV is found.

We then proceeded to obtain a measurement of the mass deposition rate from the RGS data by using the `mekal+mkcflow` model with abundances constrained to be the same in both components. As for the EPIC data analysis, the temperature range of the `mkcflow` component was fixed to 0.3–3.0 keV. We found no statistically significant improvement with respect to the single-temperature model ($C_{\rm stat}$/d.o.f. = 1977/1951). The best-fit ambient hot temperature was $kT_{\rm hot} = (6.3 \pm 0.5)$ keV with a metal abundance of $Z = 0.43 \pm 0.09\ Z_\odot$. The best-fit value for the mass deposition rate was $\dot{M} = 122^{+343}_{-122}\ M_\odot\ \mathrm{yr}^{-1}$. The 90% upper limit on the mass deposition rate was $682\ M_\odot\ \mathrm{yr}^{-1}$.

More complicated models, such as the one including a set of `mkcflow` models, are not constrained by the RGS data. However, we were able to obtain constraints on the abundance of metals other than iron using a `vmekal` model. We found $Z_{\rm Mg} = (0.53 \pm 0.24)\ Z_\odot$, $Z_{\rm Si} = (0.66 \pm 0.15)\ Z_\odot$, and $Z_{\rm S} = (0.33 \pm 0.25)\ Z_\odot$. The use of `vmekal` provides a slightly lower upper limit on the mass deposition rate: $\dot{M} = 103^{+345}_{-103}\ M_\odot\ \mathrm{yr}^{-1}$, with a 90% upper limit of $590\ M_\odot\ \mathrm{yr}^{-1}$. Best-fit temperatures are left unchanged.

We applied the same analysis to the RGS spectrum extracted from a smaller region with a width of 15″. We obtained very similar results, with small differences, the largest being a lower value of about 1σ of the ambient hot temperature, which was meaured to be $kT_{\rm hot} = 5.7^{+0.6}_{-0.3}$ keV. As for the mass deposition rate, we found a 1σ upper limit of $\dot{M} = 470\ M_\odot\ \mathrm{yr}^{-1}$, with a 90% upper limit at $744\ M_\odot\ \mathrm{yr}^{-1}$. Therefore, the RGS spectral analysis provides similar results for the two different extraction regions.

To summarize, the analysis of the RGS data only provided upper limits to the global mass deposition rate, in agreement with the values found with the analysis of the EPIC pn data, and also consistent with those found with EPIC MOS within less than 2σ. The better agreement with EPIC pn analysis is expected on the basis of the cross-calibration status of XMM instruments: the agreement between EPIC pn and RGS is currently within a few percent as a result of the combined effect of the RGS contamination model plus the improved pn redistribution model (Stuhlinger 2010).

At the same time, we remark that the comparison between the values of $\dot{M}$ obtained from the two RGS extraction regions and the EPIC pn extraction region allows us to conclude that our choice of the extraction radius for EPIC data was adequate for sampling the possible cold gas emission. The simple fact that $\dot{M}$ from RGS sampled in the region twice larger than that used for EPIC data is not significantly larger than the value found in the pn data confirms that no significant emission from cold gas can be found outside the 13″ radius.

4.4. Discussion of the systematics in XMM-Newton data analysis

The discrepancy among the results obtained with MOS and pn can be ascribed to the uncertain cross-calibration of the effective area among the *XMM-Newton* CCD, while there are no other sources of statistical noise that can account for a significant fraction of this discrepancy. This difference is persistent despite the recent model for the MOS contamination introduced in the SAS release v13.5.0 (see Sembay & Saxton 2013). Since the contribution of the cold gas below 3 keV to the total emission in the extracted region is about 3% in the 0.5−2.0 keV energy range and about 5% in the 0.5−1.0 keV range, an uncertainty in the

effective area of the same order may severely affect the measurement of the cold gas.

A first way to estimate the calibration uncertainty is to compare our results with the results obtained by applying the correction CORRAREA to the response area of the EPIC detectors based on the results of Read et al. (2014). The CORRAREA calibration is based on an extensive cross-calibration study of 46 non-piled-up sources extracted from the 2XMM EPIC Serendipitous Source Catalogue (Watson et al. 2009). This phenomenological correction is meant to bring into agreement the broadband fluxes measured by EPIC-MOS and EPIC-pn. We obtained an estimate of the uncertainty on $\dot{M}$ values associated to uncertainties in the EPIC response areas by comparing the best-fit values obtained with and without the CORRAREA correction. The best-fit values of $\dot{M}$ are 1% and 5% higher when applying the CORRAREA correction for MOS and pn data, respectively. This is far from the factor of 3 needed to bring $\dot{M}$ from MOS and pn into agreement. Therefore we conclude that the measurement of cold gas in the spectra of the Phoenix cluster is significantly affected by the calibration of the EPIC detectors at a level beyond that probed by Read et al. (2014).

We also included the energy range $0.3-0.5$ keV to investigate possible effects associated with this low-energy band. Although the calibration is even more uncertain in this range, the inclusion of the lowest energies may help to increase the relative contribution of the cold gas. However, when we repeated our fits on the $0.3-10$ keV energy range, we did not find any significant difference with respect to the results described in Sect. 4.2.

We also explored the possibility that data taken in different epochs may have a different calibration. However, when we excluded the shortest Obsid, which was acquired two years earlier than most of our data on the Phoenix, the best-fit values were only affected by a negligible amount.

A main source of uncertainty in the soft band is the Galactic column density. The possible presence of unnoticed fluctuations in the Galactic neutral hydrogen column densities on scales smaller than the resolution of Kalberla et al. (2005) may reach $10-40\%$ on scales of ~1 arcmin (Barnes & Nulsen 2003). Therefore, we considered a systematic uncertainty in our best-fit values of $\dot{M}$ assuming a maximum variation of NH_{Gal} by 40%. The typical effect is that the best fit is obtained for the highest allowed value of NH_{Gal}, and this implies that much more cold gas can be allocated. Specifically, if we allow the Galactic absorption to vary up to $NH_{Gal} = 2.13 \times 10^{20}$ cm^{-2}, we find $\dot{M} = 900(-390 + 110)_{stat}(-130 + 250)_{syst}$ $M_{\odot}$ yr^{-1} from the analysis of the MOS data with a single mkcflow model in the temperature range $0.3-3.0$ keV. This value is 45% higher than that obtained with the NH_{Gal} value of Kalberla et al. (2005) at the position of the cluster. A similar effect is found for the other fits, including those with the multi-component mkcflow model. If, on the other hand, we leave NH_{Gal} free to vary, we find best-fit values of $NH_{bestfit} = (2.2 \pm 0.8) \times 10^{20}$ cm^{-2}, which is very close to the upper bound we assumed for NH_{Gal}. The analysis of the EPIC pn data, with the same values of NH_{Gal}, provides $\dot{M}$ values 2.3 and 3 times higher for $NH_{Gal} = 2.13$ and 2.2×10^{20} cm^{-2}, respectively, which considerably reduces the discrepancy between the MOS and pn analysis. However, when the Galactic absorption is left free, the best-fit value is $NH_{Gal} = (0.8 \pm 0.2) \times 10^{20}$ cm^{-2}, which in turn provides much lower values of $\dot{M}$ than the standard analysis. Therefore, we conclude that there are no hints for a plausible variation of NH_{Gal} that can significantly change our results, including the discrepancy between the best-fit values of $\dot{M}$ found between MOS and pn data.
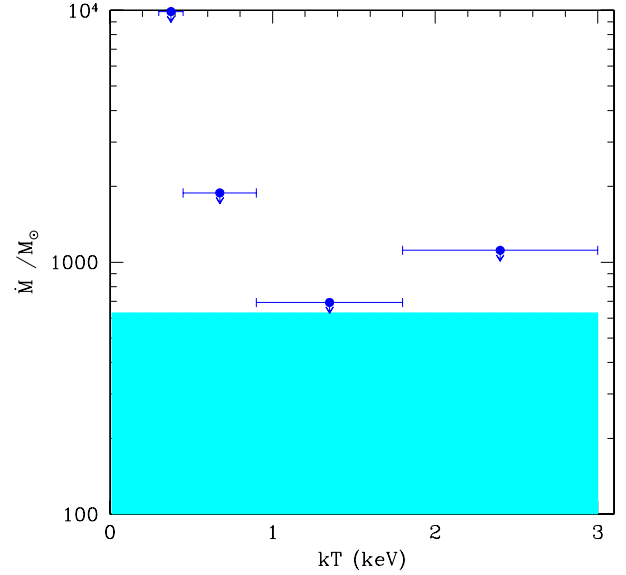
Fig. 7. Mass deposition rate $\dot{M}$ as a function of the temperature from the analysis of the ACIS-I *Chandra* data of Phoenix within 30 kpc from the center. The AGN emission has been removed (inner 1.5 arcsec). The results have been obtained with a multi-temperature mkcflow plus a mekal model for the hot component. Arrows refer to 1σ upper limits. The shaded area shows the 1σ upper limit based on the analysis of a single-temperature mkcflow model in the $0.3-3.0$ keV temperature range plus a mekal model for the hot component.

4.5. Comparison with spectral results on the core region from Chandra data

We repeated the same fits on the *Chandra* data available in the archive as of December 2014. The photometry in the inner 30 kpc, corresponding to 4.5 arcsec, excluding the central AGN, amounts to 1510 net counts in the $0.5-7.0$ keV energy band. This is usually not sufficient to provide robust constraints on the amount of cold gas in nearby clusters, and it would be even less effective at the redshift of Phoenix. Nevertheless, we performed our spectral analysis as for the *XMM-Newton* data. The single-temperature mkcflow model in the temperature range $0.3-3.0$ keV provides a 1σ upper limit of $630(-85 + 60)_{syst}$ $M_{\odot}$ yr^{-1} or a 2σ upper limit of $1130(-150 + 1100)_{syst}$ $M_{\odot}$ yr^{-1}, where the systematic uncertainty corresponds to $0.45 < Z_{cold} < 1.4$ $Z_{\odot}$. The hot gas temperature is $kT_{hot} = 7.2^{+1.3}_{-0.6}$ keV, within 1σ from the value found in *XMM-Newton* analysis and in the overall temperature profile of the *Chandra* data. We recall that we did not fit the AGN since its emission was removed from the spectrum thanks to the *Chandra* angular resolution.

Despite the low S/N of the *Chandra* data (almost two orders of magnitude fewer photons than for the combined *XMM-Newton* spectra), and the high redshift of the Phoenix cluster, we also performed the fit with a multi-component mkcflow model. Temperature and metallicity of the hot gas component were the same as in the previous fit, while $Z_{cold} = 1.0$ $Z_{\odot}$. As expected, we obtained little additional information. The results are summarized in Fig. 7, where we can conclude that the strongest constraints on $\dot{M}$ mostly comes from the gas between 0.9 and 1.8 keV. This means that *Chandra* upper limits are consistent with a mass deposition rate of about ~1000 $M_{\odot}$ yr^{-1}. We remark, however, that deeper *Chandra* data are expected to provide much stronger constraints.
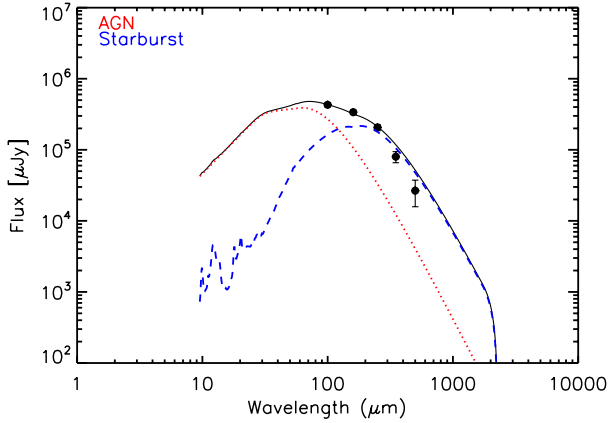
Fig. 8. Spectral energy distribution of the BCG of Phoenix in the FIR from the PACS (100 and 160 μm) and SPIRE (250, 350, 500 μm) instruments onboard the *Herschel* Space Observatory. The red dotted line and the blue dashed line show the best fit to the SED for the AGN and starburst template, respectively.

5. Exploring the connection between SFR and global $\dot{M}$

We inspected available FIR data on the Phoenix cluster to better constrain the SFR. The BCG has been observed in the FIR with the PACS (100 and 160 μm) and SPIRE (250, 350, 500 μm) instruments onboard the *Herschel* Space Observatory (Pilbratt et al. 2010). *Herschel* data bracket the critical peak of FIR emission of high-redshift galaxies, providing a direct, unbiased measurement of the dust-obscured SFR. We performed aperture photometry assuming an aperture radius of 6 and 9 arcsec for 100 and 160 μm, respectively, while for SPIRE we used PSF fitting. The five data points from *Herschel* instruments provide the SED shown in Fig. 8.

We investigated the contribution of the AGN component to the FIR emission using the program DECOMPIR (Mullaney et al. 2011), an SED model-fitting software that aims to separate the AGN from the host star-forming (SF) galaxy. The AGN component is an empirical model based on observations of local AGNs, whereas the five starburst models were developed to represent a typical range of SED types, with an extrapolation beyond 100 μm using a gray body with emissivity β fixed to 1.5. The best-fitting model obtained with DECOMPIR confirms at least a 50% contribution of the AGN to the total SED flux, as shown in Fig. 8. The AGN clearly dominates the FIR emission. The IR luminosity for the starburst component (best described by the model SB5 in Mullaney et al. 2011) is measured to be $L_{IR} = 3.1 \times 10^{12} L_\odot$. Assuming a Salpeter IMF, this luminosity corresponds to a SFR of 530 $M_\odot$ yr^{-1} with a typical error of 15%, which is lower than the value found by McDonald et al. (2013) at 3σ c.l. The total luminosity given by the best fit is $L_{IR} = 2.09 \times 10^{13} L_\odot$, with the AGN component contributing by 86%. Taken at face value, this revised estimate of the SFR is in very good agreement with the mass deposition rate found with the analysis of the EPIC MOS data, while is still inconsistent at about 3σ c.l. with the mass deposition rate found with EPIC pn analysis.

6. Conclusions

We analyzed the X-ray data taken with a 220 ks exposure of *XMM-Newton* on the Phoenix cluster. We focused on cold gas in the core by selecting a circle of 13.5 arcsec centered on the BCG in the XMM image and a strip with a width corresponding to 90% of the PSF in the RGS data. Our immediate goal was to constrain the actual mass-deposition rate associated with the residual cooling flow, with the aim of understanding whether this may be directly linked to the current massive starburst observed in the BCG. We combined *XMM-Newton* data with shallow *Chandra* data, particularly to model the hard emission of the central absorbed AGN, which cannot be removed from the *XMM-Newton* data alone. Our results are summarized as follows:

- We measured an average mass-deposition rate of $\dot{M} = 620(-190 + 200)_{stat}(-50 + 150)_{syst}$ $M_\odot$ yr^{-1} and $\dot{M} = 210(-80 + 85)_{stat}(-35 + 60)_{syst}M_\odot$ yr^{-1} in the 0.3−3.0 keV temperature range from the analysis of the MOS and pn data, respectively. These values are dominated by the cold gas in the energy range 1.8−3.0 keV, while only upper limits can be obtained at temperatures below 1.8 keV. The upper limits to the global mass deposition rate below 1.8 keV appear to be consistent with an SFR of ~800 $M_\odot$ yr^{-1}, as measured in the BCG by McDonald et al. (2013), from the EPIC MOS data analysis within 1σ, while the upper limits on $\dot{M}$ measured from EPIC pn data at temperatures below 1.8 keV are significantly lower (more than 3σ) than the SFR measured in McDonald et al. (2013).
- Considering the temperature range 0.3−1.8 keV, we found that MOS data analysis is consistent with $\dot{M} \sim 1000$ within 1σ, while the pn data provide $\dot{M} < 400$ $M_\odot$ yr^{-1} at 3σ c.l.
- Since the discrepancy between the MOS and pn data analyses cannot be explained on the basis of currently known cross-calibration uncertainties between the two instruments nor of other sources of statistical noise, we argue that additional calibration problems between EPIC instruments still need to be understood and properly treated. The contribution of the cold gas with an average mass-deposition rate of ~600 $M_\odot$ yr^{-1} in the EPIC data is about 5% in the energy range 0.5−1.0 keV for our extraction region. This implies that any calibration uncertainty on the same order strongly affects the data. This conclusion is valid in the framework of the isobaric cooling model that we assumed here. At present, we are unable to discuss whether the assumptions of different physical models for describing the cooling of the gas can change the picture and mitigate the difference between MOS and pn analysis.
- No line emission from ionization states below Fe XXIII is seen above 12 Å in the RGS spectrum, and the amount of gas cooling below ~3 keV has a formal best-fit value for the mass deposition rate of $\dot{M} = 122^{+343}_{-122}$ $M_\odot$ yr^{-1}. This result was confirmed by a direct comparison of the Phoenix RGS spectrum with A1835 in the overlapping spectral range. This means that the mass deposition rate from RGS analysis is lower than the SFR of McDonald et al. (2013) in the BCG at the 2σ c.l.
- Current *Chandra* data (from a short exposure of ~10 ks) agree with our *XMM-Newton* analysis, but do not provide meaningful constraints on $\dot{M}$. Deeper *Chandra* data, thanks to the high angular resolution, are expected to provide tighter constraints to the global mass deposition rate.
- A careful analysis of the FIR SED based on *Herschel* data provided a value for the SFR in the BCG of 530 $M_\odot$ yr^{-1} with an uncertainty of 15%. This revised estimate of the SFR agrees very well with the $\dot{M}$ from EPIC MOS data and is consistent within 1σ with $\dot{M}$ from the RGS analysis, while still inconsistent at more than 3σ with the mass deposition

rate found in EPIC pn data. Our revised SFR therefore does not significantly change the comparison between SFR and the global $\dot{M}$ in the Phoenix cluster.

To summarize, the range of $\dot{M}$ allowed by *XMM-Newton* data from EPIC MOS is consistent with the SFR observed in the BCG, while EPIC pn and RGS data analyses suggest a mass deposition rate of about $\sim SFR/3$, and the derived upper limit is inconsistent with the observed SFR at least at the 2σ level for RGS, and more than 3σ for EPIC-pn. As a consequence, our results do not provide a final answer on the possible agreement between the mass deposition rate of isobaric cooling gas in the core and the observed SFR in the BCG. As recently shown by Molendi et al. (in prep.), $\dot{M}$ is often measured to be significantly lower than the global SFR in central cluster regions for several strong cool-core clusters. These findings suggest that cooling flows may be short-lived episodes, efficient in building the cold mass reservoir that, on a different timescale and possibly with some delay, triggers the SFR in the BCG. To investigate whether this also occurs in the Phoenix cluster, or whether the Phoenix cluster actually hosts the highest cooling flow observed so far with $\dot{M} \simeq SFR$, we must wait for a deep, high-resolution, spatially resolved X-ray spectral analysis to remove the stronger emission from the surrounding hot gas as best possible.

References

Arnaud, M., Pratt, G. W., Piffaretti, R., et al. 2010, A&A, 517, A92
Asplund, M., Grevesse, N., & Sauval, A. J. 2005, in Cosmic Abundances as Records of Stellar Evolution and Nucleosynthesis, eds. T. G. Barnes III, & F. N. Bash, ASP Conf. Ser., 336, 25
Barnes, D. G., & Nulsen, P. E. J. 2003, MNRAS, 343, 315
Blanton, E. L., Randall, S. W., Clarke, T. E., et al. 2011, ApJ, 737, 99
Böhringer, H., Belsole, E., Kennea, J., et al. 2001, A&A, 365, L181
Böhringer, H., Matsushita, K., Churazov, E., Ikebe, Y., & Chen, Y. 2002, A&A, 382, 804
Cowie, L. L., & Binney, J. 1977, ApJ, 215, 723
De Grandi, S., Santos, J. S., Nonino, M., et al. 2014, A&A, 567, A102
Ettori, S., Gastaldello, F., Leccardi, A., et al. 2010, A&A, 524, A68

Ettori, S., Donnarumma, A., Pointecouteau, E., et al. 2013a, Space Sci. Rev., 177, 119
Ettori, S., Gastaldello, F., Gitti, M., et al. 2013b, A&A, 555, A93
Fabian, A. C. 1994, ARA&A, 32, 277
Fabian, A. C., & Nulsen, P. E. J. 1977, MNRAS, 180, 479
Fabian, A. C., Sanders, J. S., Allen, S. W., et al. 2003, MNRAS, 344, L43
Fabian, A. C., Sanders, J. S., Taylor, G. B., et al. 2006, MNRAS, 366, 417
Fabian, A. C., Sanders, J. S., Allen, S. W., et al. 2011, MNRAS, 418, 2154
Gaspari, M., Brighenti, F., D'Ercole, A., & Melioli, C. 2011a, MNRAS, 415, 1549
Gaspari, M., Melioli, C., Brighenti, F., & D'Ercole, A. 2011b, MNRAS, 411, 349
Gonzalez, A. H., Sivanandam, S., Zabludoff, A. I., & Zaritsky, D. 2013, ApJ, 778, 14
Kaastra, J. S., Ferrigno, C., Tamura, T., et al. 2001, A&A, 365, L99
Kalberla, P. M. W., Burton, W. B., Hartmann, D., et al. 2005, A&A, 440, 775
Kirkpatrick, C. C., McNamara, B. R., & Cavagnolo, K. W. 2011, ApJ, 731, L23
Komatsu, E., Smith, K. M., Dunkley, J., et al. 2011, ApJS, 192, 18
Lin, Y.-T., Mohr, J. J., & Stanford, S. A. 2003, ApJ, 591, 749
Mathews, W. G., & Bregman, J. N. 1978, ApJ, 224, 308
Mazzotta, P., Rasia, E., Moscardini, L., & Tormen, G. 2004, MNRAS, 354, 10
McDonald, M., Bayliss, M., Benson, B. A., et al. 2012, Nature, 488, 349
McDonald, M., Benson, B., Veilleux, S., Bautz, M. W., & Reichardt, C. L. 2013, ApJ, 765, L37
McNamara, B. R., & Nulsen, P. E. J. 2012, New J. Phys., 14, 055023
McNamara, B. R., Wise, M., Nulsen, P. E. J., et al. 2000, ApJ, 534, L135
McNamara, B. R., Nulsen, P. E. J., Wise, M. W., et al. 2005, Nature, 433, 45
Molendi, S., & Pizzolato, F. 2001, ApJ, 560, 194
Mullaney, J. R., Alexander, D. M., Goulding, A. D., & Hickox, R. C. 2011, MNRAS, 414, 1082
Mushotzky, R. F., & Szymkowiak, A. E. 1988, in NATO ASIC Proc. 229: Cooling Flows in Clusters and Galaxies, ed. A. C. Fabian, 53
Navarro, J. F., Frenk, C. S., & White, S. D. M. 1996, ApJ, 462, 563
Peterson, J. R., & Fabian, A. C. 2006, Phys. Rep., 427, 1
Peterson, J. R., Paerels, F. B. S., Kaastra, J. S., et al. 2001, A&A, 365, L104
Peterson, J. R., Kahn, S. M., Paerels, F. B. S., et al. 2003, ApJ, 590, 207
Pilbratt, G. L., Riedinger, J. R., Passvogel, T., et al. 2010, A&A, 518, L1
Randall, S. W., Forman, W. R., Giacintucci, S., et al. 2011, ApJ, 726, 86
Read, A. M., Guainazzi, M., & Sembay, S. 2014, A&A, 564, A75
Sanders, J. S., Fabian, A. C., Smith, R. K., & Peterson, J. R. 2010, MNRAS, 402, L11
Santos, J. S., Tozzi, P., Rosati, P., & Böhringer, H. 2010, A&A, 521, A64
Santos, J. S., Tozzi, P., Rosati, P., Nonino, M., & Giovannini, G. 2012, A&A, 539, A105
Sembay, S., & Saxton, R. 2013, XMM-CCF-REL-0305
Silk, J. 1976, ApJ, 208, 646
Stuhlinger, M. 2010, XMM-SOC-CAL-TN-0052 http://xmm2.esac.esa.int/docs/documents/CAL-TN-0052.ps.gz
Sun, M. 2009, ApJ, 704, 1586
Tamura, T., Kaastra, J. S., Peterson, J. R., et al. 2001, A&A, 365, L87
Ueda, S., Hayashida, K., Anabuki, N., et al. 2013, ApJ, 778, 33
Watson, M. G., Schröder, A. C., Fyfe, D., et al. 2009, A&A, 493, 339
Werner, N., Zhuravleva, I., Churazov, E., et al. 2009, MNRAS, 398, 23
Williamson, R., Benson, B. A., High, F. W., et al. 2011, ApJ, 738, 139
Zhuravleva, I., Churazov, E., Schekochihin, A. A., et al. 2014, Nature, 515, 85